ADVANCED MATERIALS
www.advmat.de

Imaging the Breakdown and Restoration of Topological Protection in Magnetic Topological Insulator $MnBi_2Te_4$

Qile Li, Iolanda Di Bernardo, Johnathon Maniatis, Daniel McEwen, Amelia Dominguez-Celorrio, Mohammad T. H. Bhuiyan, Mengting Zhao, Anton Tadich, Liam Watson, Benjamin Lowe, Thi-Hai-Yen Vu, Chi Xuan Trang, Jinwoong Hwang, Sung-Kwan Mo, Michael S. Fuhrer, and Mark T. Edmonds**

Quantum anomalous Hall (QAH) insulators transport charge without resistance along topologically protected chiral 1D edge states. Yet, in magnetic topological insulators to date, topological protection is far from robust, with zero-magnetic field QAH effect only realized at temperatures an order of magnitude below the Néel temperature T_N, though small magnetic fields can stabilize QAH effect. Understanding why topological protection breaks down is therefore essential to realizing QAH effect at higher temperatures. Here a scanning tunneling microscope is used to directly map the size of exchange gap ($E_{g,ex}$) and its spatial fluctuation in the QAH insulator 5-layer $MnBi_2Te_4$. Long-range fluctuations of $E_{g,ex}$ are observed, with values ranging between 0 (gapless) and 70 meV, appearing to be uncorrelated to individual surface point defects. The breakdown of topological protection is directly imaged, showing that the gapless edge state, the hallmark signature of a QAH insulator, hybridizes with extended gapless regions in the bulk. Finally, it is unambiguously demonstrated that the gapless regions originate from magnetic disorder, by demonstrating that a small magnetic field restores $E_{g,ex}$ in these regions, explaining the recovery of topological protection in magnetic fields. The results indicate that overcoming magnetic disorder is the key to exploiting the unique properties of QAH insulators.

1. Introduction

Topological protection has become a crucial concept in the recent development of condensed matter physics.[1–4] In the quantized versions of the Hall effect (QHE), spin Hall effect (QSHE), and anomalous Hall effect (QAHE), topological protection manifests as 1D electronic edge states where scattering due to local perturbations is prohibited.[5] This opens the way toward high-temperature lossless electronic transport applications[6,7] as well as new approaches to topologically-protected fault-tolerant quantum computing.[8,9] These technologies require robust topologically protected edge channels, but in electronic devices, this protection is often observed to break down. Breakdown of the QHE due to disorder, temperature, and current has been understood within scaling theory,[10] and was a fundamental development in the understanding of continuous quantum phase transitions.[11] The microscopic origins of

Q. Li, I. Di Bernardo, J. Maniatis, D. McEwen, A. Dominguez-Celorrio, M. T. H. Bhuiyan, M. Zhao, L. Watson, B. Lowe, T.-H.-Y. Vu, C. X. Trang, M. S. Fuhrer, M. T. Edmonds
School of Physics and Astronomy
Monash University
Clayton, Victoria 3168, Australia
E-mail: qile.li@monash.edu; mark.edmonds@monash.edu

Q. Li, I. Di Bernardo, D. McEwen, A. Dominguez-Celorrio, M. Zhao, A. Tadich, L. Watson, B. Lowe, C. X. Trang, M. S. Fuhrer, M. T. Edmonds
ARC Centre for Future Low Energy Electronics Technologies
Monash University
Clayton, Victoria Australia

I. Di Bernardo, A. Tadich
Instituto Madrileño de Estudios Avanzados en Nanociencia (IMDEA-Nanociencia)
Madrid 28049, Spain

M. Zhao
Australian Synchrotron
Clayton, Victoria 3168, Australia

J. Hwang, S.-K. Mo
Advanced Light Source
Lawrence Berkeley National Laboratory
Berkeley, CA 94720, USA

J. Hwang
Department of Physics and Institute of Quantum Convergence Technology
Kangwon National University
Chuncheon 24341, Republic of Korea

M. T. Edmonds
ANFF-VIC Technology Fellow
Melbourne Centre for Nanofabrication
Victorian Node of the Australian National Fabrication Facility
Clayton, Victoria 3168, Australia

The ORCID identification number(s) for the author(s) of this article can be found under https://doi.org/10.1002/adma.202312004

DOI: 10.1002/adma.202312004

disorder-induced QHE breakdown are still a vibrant area of investigation, with new developments in graphene showing unique aspects of backscattering in the presence of both electron- and hole-like edge channels.[12,13] The QSHE is robust to non-magnetic disorder at zero temperature,[14] but magnetic disorder can cause scattering at finite temperatures,[15] with a quantum phase transition from helical liquid to insulator under strong interactions.[14] In contrast, the chiral quantum anomalous Hall (QAH) edge channel supports a unidirectional flow of electrical current that should be robust to any potential perturbations smaller than the exchange energy gap $E_{g,ex}$ which is opened in the surface-state of a thin film 3D topological insulator (TI) via long-range magnetic order.[16,17] Despite this, the breakdown of topological protection is ubiquitously observed at far lower temperatures than $E_{g,ex}/k_B$ or T_N, where k_B is the Boltzmann constant. In dilute magnetic doped topological insulators, this is thought to be due to magnetic disorder, leading to non-uniform magnetization and a fragile QAHE that is only observable at extremely low temperatures (<1 K).[18,19]

Intrinsic stoichiometric magnetic topological insulators (MTIs) which possess both non-trivial topology and intrinsic magnetism, for example, $MnBi_2Te_4$[20,21] should in principle circumvent the issues associated with dilute magnetic doping. Promisingly, odd layers of $MnBi_2Te_4$ in the 2D limit host QAH states,[22] leading to observation of the QAHE at 1.4 K, with the temperature increasing to 6.5 K under the application of an external magnetic field.[23] Yet, this value is still substantially lower than T_N = 25 K and the activation energy extracted from transport measurements of ΔE = 0.64 meV is two orders of magnitude smaller than the predicted $E_{g,ex}$ = 70 meV (800 K). Furthermore, QAHE is not routinely observed in ultra-thin odd-layer $MnBi_2Te_4$ samples or quantization is only observable in a large perpendicular magnetic field.[24] These results hint at the presence of various types of surface disorders that act to suppress the $E_{g,ex}$[25] and destroy QAHE.

Understanding the mechanism of topological breakdown requires direct measurement of the interplay between surface disorder, local fluctuations in $E_{g,ex}$, and the chiral edge state with atomic-scale precision. Low-temperature scanning tunneling microscopy and spectroscopy (STM/STS) has been previously used to probe band gap fluctuations and edge states in other 2D materials.[2,18,28–31] To date, most STM/STS measurements on $MnBi_2Te_4$ have been performed on bulk crystals and have focused on point defects.[26–28] Little attention has been paid to ultra-thin films of $MnBi_2Te_4$ and the mechanisms of topological protection breakdown and suppression of QAHE. A recent report suggests the connection between local magnetic Mn_{Bi}, Bi_{Mn} anti-site defects (notation X_Y means a X ion replaces a Y ion in the lattice) and collapse of the exchange gap in high defect regions, but did not measure the gap fluctuations over large areas to understand possible short-range behavior from magnetic disorder, how disorder interacts with the chiral edge state[29] or how the disorder effects respond to a magnetic field. Thus, the mechanism by which topological protection is destroyed, as well as how it recovers in B field, are still not understood.

In this work, we utilize magnetic field STM/STS to study the origin of QAHE suppression in 5 septuple layer (SL) $MnBi_2Te_4$. We directly measure spatial fluctuation of $E_{g,ex}$ and importantly observe the electronic overlap of the gapless edge state with gapless metallic bulk states, providing the route to breakdown of the QAHE. Finally, we demonstrate that by applying a magnetic field well below the spin-flop transition, we are able to restore the exchange gap in the gapless regions, explaining the recovery of QAHE in small magnetic fields.

2. Results and Discussion

Figure 1a,b presents the crystal structure of one septuple layer (SL) $MnBi_2Te_4$. Lattice constants, magnetic moments, and possible lattice defects are labeled. Within each SL, intra-layer Mn^{2+} ions are coupled through ferromagnetic interaction. Between two adjacent SLs, two Mn^{2+} atomic layers are coupled through anti-ferromagnetic (AFM) interaction, resulting in thickness-dependent magnetic properties. We grow high-quality epitaxial ultra-thin $MnBi_2Te_4$ using molecular beam epitaxy (MBE) on Si (111)–7 × 7. Due to interfacial charge transfer as a result of the different work functions of *p*- and *n*-type silicon (111), the doping level in $MnBi_2Te_4$ films can be tuned. This allows for STM/STS measurements performed on $MnBi_2Te_4$ on *p*-type Si(111) which has the Fermi energy in the exchange gap, whilst for angle-resolved photoemission spectroscopy (ARPES) measurements performed on $MnBi_2Te_4$ on *n*-type Si(111), the films are electron-doped, allowing the Dirac electron band to be observed. See Experimental Section for growth details. Structural characterization as well as the role of substrate and doping can be found in Figures S1 and S2, Supporting Information. Figure S1b, Supporting Information shows a typical large-area STM topography scan with coexisting regions of 4 and 5 SL $MnBi_2Te_4$ islands that are atomically flat, along with small pinholes of bare substrate. Figure 1c shows a 20 × 20 nm atomic resolution STM image revealing the expected 1 × 1 atomic surface structure with a lattice constant of 4.3 Å. Several different defects are present; bright spots on the surface correspond to negatively charged Bi_{Te} point defects and the dark triangles are Mn_{Bi} defects. Similar defects have been observed in Cr, Mn-doped 3D TIs.[19,30,31] The third defect type—Bi_{Mn} (located in the middle of each SL) is not directly visible in Figure 1c but is presented in Figure S3, Supporting Information.

Figure 1d shows an ARPES spectrum of a 5 SL $MnBi_2Te_4$ thin film grown on *n*-type Si (111) taken at 8 K and photon energy of 50 eV along ΓM direction where a Dirac cone is clearly visible near the Fermi level. The strong spectral weight near Γ in the Dirac point region could be due to Te-orbital-related matrix elements[32,33] or be the result of bandgap fluctuations as the spectral signal is averaged over the beam spot size (100 × 100 µm). The gapped Dirac cone in the ARPES spectrum along ΓM direction can be modeled with a hyperbola model: $E(k) = D \pm \sqrt{v^2k^2 + \Delta^2}$ where D is the doping level, v the band velocity, k the wavevector and Δ the exchange gap.[32] The doping level and band velocity can be estimated based on the band dispersion extracted from momentum distribution curve analysis, where a series of horizontal profiles from the spectrum are fit with two Lorentzian peaks to extract the band dispersion. With the estimated doping level and band velocity, we can model the Dirac cone if we know the exchange gap. However, the strong spectral weight prevents us from extracting the exchange gap accurately. To demonstrate the possibility of exchange gap fluctuations, we fit the ARPES spectrum in Figure 1d with three possible scenarios of different exchange gap sizes (red curve: full band gap $E_{g,ex}$

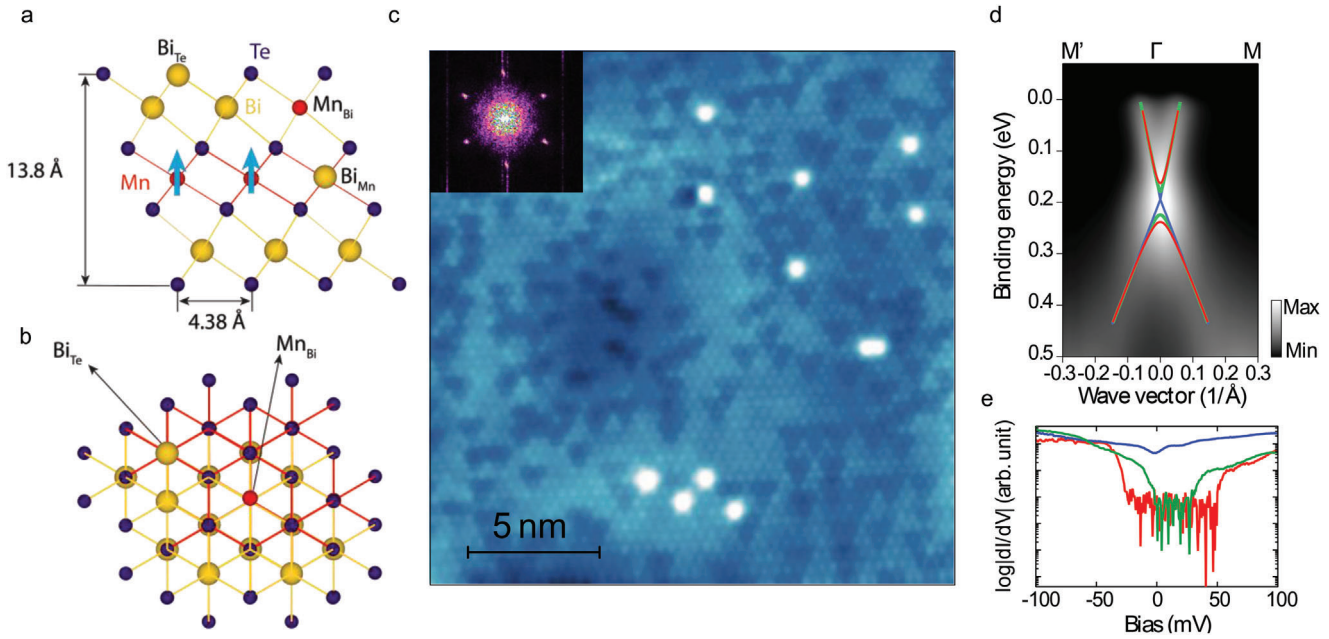

Figure 1. Characterization of epitaxial ultra-thin $MnBi_2Te_4$ and overall electronic structure from ARPES. a,b) Crystal structures of a septuple layer of $MnBi_2Te_4$. a) Side view of the lattice with lattice constants, atom species, and defects labeled. The magnetic moments on Mn^{2+} ions are marked with blue arrows. b) Top view of the lattice. c) Atomic resolution image (−2 V, 180 pA) of a flat 20 × 20 nm area where Mn_{Bi} (dark triangles) and Bi_{Te} (bright dots) defects are clearly visible. The insert shows the fast Fourier transformed image of the same area (note the spots corresponding to 1 × 1 surface atomic structure). d) Angle-resolved photoemission spectrum (photon energy 50 eV) of five-layer $MnBi_2Te_4$ along Γ-M where the fully gapped ($E_{g,ex}$ = 70 meV) band dispersion is marked by a red curve. Green and blue curves are illustrations of possible reduced gap and gapless dispersions ($E_{g,ex}$ = 35 and 0 meV respectively). e) dI/dV spectra taken at different locations on the same terrace of 5 SL $MnBi_2Te_4$ (−0.2 V, 400 pA) showing gapless (blue curve), reduced gap (green curve) and fully gapped (red curve) dI/dV spectra from different regions on the same terrace.

= 70 meV extracted from energy distribution curve analysis,[32] green curve: reduced $E_{g,ex}$ = 35 meV, blue curve: gapless $E_{g,ex}$ = 0 meV limit). The models for these three scenarios show good agreement to the spectrum and binding energy of the strong spectral feature coincides with Dirac bands in the gapless and reduced gap models.

To properly understand the $E_{g,ex}$ distribution, we use STS to measure the dI/dV spectrum (the differential conductance dI/dV as a function of sample bias V) which is proportional to the local density of states (LDOS) at energy $E_F + eV$, where e is the elementary charge. Figure 1e shows three typical STS on the same SL terrace. The size of $E_{g,ex}$ changes drastically with location: the red STS curve corresponds to $E_{g,ex}$ = 70 meV, the green curve shows a reduced band gap $E_{g,ex}$ = 35 meV, and the blue curve is consistent with a gapless ($E_{g,ex}$ = 0 meV) spectrum (see Figures S4 and S5, Supporting Information for details on extracting exchange gap and parking bias/set point current dependent measurements demonstrating minimal tip-induced band bending). All spectra in Figure 1e were taken more than 5 nm away from step edges in order to exclude effects from edge states.

Before turning to the origin of the exchange gap fluctuation, we probe the step edge between 4 and 5 SL $MnBi_2Te_4$ to verify the presence of the conductive edge state, a consequence of topological protection and signature of a quantum anomalous Hall insulator (QAHI). In principle, the edge state exists at the edge of the sample where the height profile on the sample drops from 5 SL thickness to the underlying substrate. However, due to a variety of growth and measurement practicalities, measuring the edge state on the sample edge with STM is extremely challenging. Therefore, instead, we probe the edge state on the 5 SL (Chern number of ± 1) to 4 SL (Chern number of 0) step edge enabled by the unique thickness-dependent topological property of $MnBi_2Te_4$.[22] Since the edge state appears on the boundary between two phases with different topological invariants, the physics of the edge state on the terrace edge is equivalent to that of the edge state on the sample edge.

Figure 2a,b shows STM topography and dI/dV maps taken across two different 4 to 5 SL step edges on two separately grown $MnBi_2Te_4$ thin films. Since the chiral edge state exists within the exchange gap, the sample bias was tuned into the exchange gap to image the edge state. The lower panel of Figure 2a shows a dI/dV map taken at +25 mV: a pronounced increase in dI/dV signal is observed that is localized at the step edge (which is marked by a red dashed line), indicating a conductive edge state. This conductive edge state is mostly continuous, but has strong hybridization between the edge state and some metallic states in the interior of the terrace and is not spatially isolated. In the following discussion, we will call these unexpected metallic states "metallic bulk states" where "bulk" will always refer to the interior of the terrace as opposed to "boundary" – the step edge. By performing a connectivity analysis (Figure S6, Supporting Information), we have found an isolated edge state in the bottom region and a strongly coupled edge state in the middle region. The edge state becomes weakly coupled to the bulk states in the upper region. The second edge presented in Figure 2b shows another step edge consisting of a 5SL edge (orange arrow) and sub-step edge (excluded

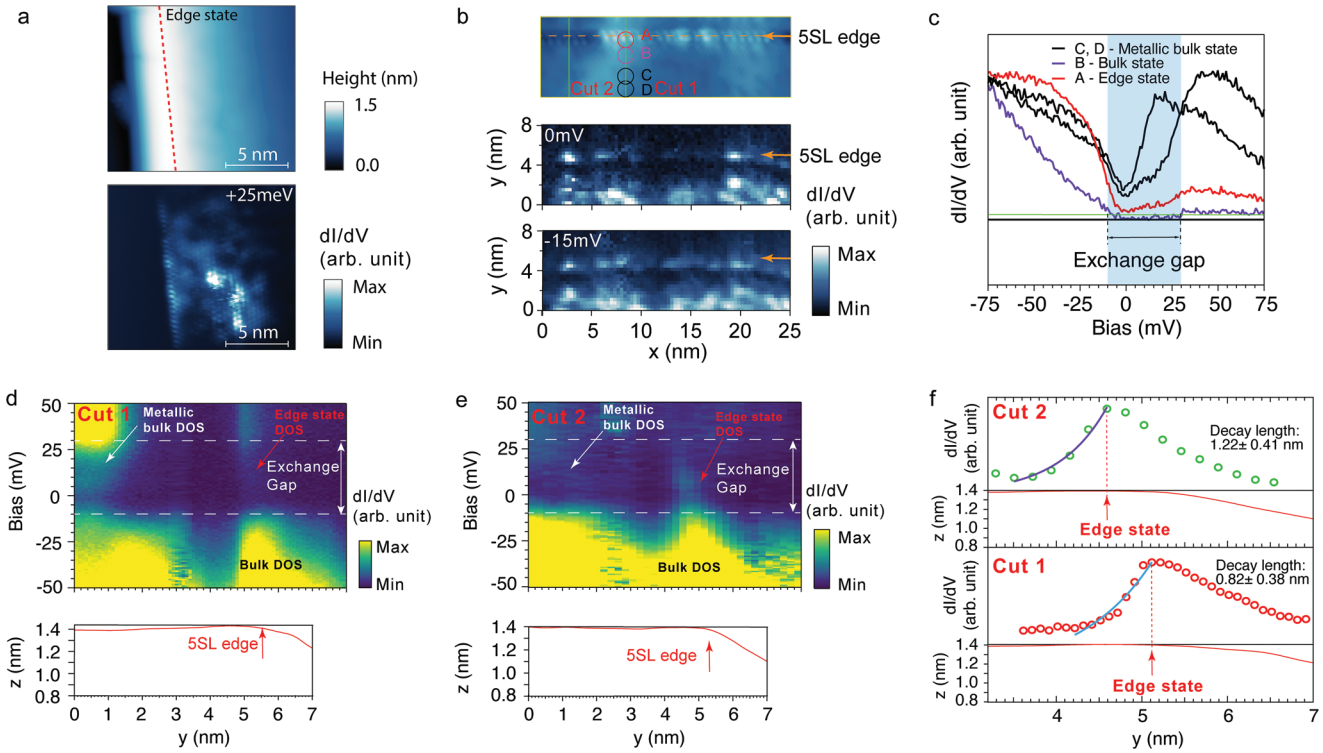

Figure 2. Visualizing the gapless edge state and its coupling to metallic bulk states. a,b) STM topography taken at −1 V (upper panels) and d*I*/d*V* maps (lower panels) taken across two different 4 to 5 SL $MnBi_2Te_4$ step edges. a) d*I*/d*V* map at +25 mV bias (40 pA) shows a pronounced increase in intensity at the edge state and its strong coupling to bulk metallic states. The location of the edge state is marked by a red dashed line. b) d*I*/d*V* maps (−0.15 V, 400 pA) at 0 and −15 mV bias show the spatial distribution of the edge state taken across a step edge and how the edge state is isolated from the metallic bulk states. The positions of the 5SL edge are marked with orange arrows. c) d*I*/d*V* spectra (−0.15 V, 400 pA) taken from edge state region A (red circle), metallic bulk region C, D (black circle), and normal bulk region B (purple circle) as marked in (b). d,e) d*I*/d*V* spectra (−0.15 V, 400 pA) and height profile taken across the edge from paths marked by green lines in (b). The horizontal axis of the spectra is aligned with the height profile. The edge state is marked by a red arrow and other in-gap peaks are attributed to metallic bulk states which are marked by white arrows. The white horizontal dashed line shows the range of exchange gap which is the same as the shaded region in (c). f) d*I*/d*V* intensity averaged in the exchange gap and plotted as a function of distance in *y*–direction showing exponential decay. The height profiles of the two cuts are shown below the d*I*/d*V* profiles respectively where the intensity maximum of the edge state is marked.

in the figure). The sub-step edge structure has also been observed in previous STM studies on $MnBi_2Te_4$ thin films.[29] The middle and lower panels of Figure 2b show d*I*/d*V* maps taken at 0 and −15 mV: that also show a pronounced increase in d*I*/d*V* signal that is localized at the step edge. At bias outside the exchange gap (−15 mV), this edge state is weakly coupled to the bulk state with finite spectral weight between the edge channel and the gapless bulk states. As the bias moves into the exchange gap (0 mV), the edge states become spatially isolated unlike the edge state presented in Figure 2a. We have included more d*I*/d*V* maps at other voltage bias, see Figure S7, Supporting Information to demonstrate the decoupled edge channel in the exchange gap. We must point out that the spectral intensity along the edge in Figure 2b seems to be disconnected, which has been also observed in previous reports on topological edge states of $MnBi_2Te_4$,[34] its related heterostructure with Bi_2Te_3,[35] as well as the 2D topological insulator WTe_2.[36] It may arise due to local roughness and structural disorder along the edge. Furthermore, we have also performed a similar d*I*/d*V* map on a 4SL to 3SL edge, and no spectral intensity is observed (Figure S8, Supporting Information), indicating the 1D edge state could be only present on the odd-layer SL $MnBi_2Te_4$ that is buried underneath the step edge which is very difficult to probe from the surface. For a perfect QAHI there should be a well-defined suppression of the bulk LDOS within the exchange gap, but we observe bulk regions well away from the edge that also show strong LDOS at the same energy, indicating the coupling between edge state and metallic bulk regions. To confirm that some metallic bulk regions are indeed metallic, in Figure 2c we measure d*I*/d*V* spectra corresponding to the edge state (red curve) at point A, normal bulk states (purple curve) at point B, and metallic bulk states (black curve) at point C, D in Figure 2b. The normal bulk region right next to the edge shows the expected insulating behavior with $E_{g,ex} = 40$ meV, but the d*I*/d*V* spectra at both the edge and within these metallic bulk state regions are quite different, with states filling the entire bulk gap. The metallic bulk states have much stronger spectral intensity above zero bias in the conduction band range, and the STS curves resemble the density of states (DOS) of a gapless Dirac cone which is essentially a 2D topological surface state.[37] This indicates a continuous metallic percolative path for electron transport from the edges through the bulk. Figure 2d,e shows spatial d*I*/d*V* profiles as a function of distance away from the edge measured along the two green lines in Figure 2b (labeled as Cut 1 and Cut 2) that demonstrate the extended nature of the edge state feature along

the step edge located at 5 nm, as marked by the red arrow. The other spectral intensity between 0 and 2 nm is clearly separated from the edge state, and we assign it to the metallic bulk states, marked by a white arrow. Figure 2f shows the summed dI/dV intensity (red curve extracted from Figure 2d; green curve extracted from Figure 2e) within the exchange gap. Moving away from the edge shows the expected exponential decay for a 1D topologically non-trivial edge state.[2,38] The extracted exponential decay lengths are 0.82 ± 0.38 nm and 1.22 ± 0.41 nm. Although the observed edge state appears to be isolated from the metallic bulk states, the small spatial separation (less than 3 nm) implies fragile edge state conduction. The observation of a 1D edge state on two different step edges (Figure 2 and additional STS data presented in Figure S9, Supporting Information), suggests the 1D edge state exists on the 5SL to 4SL edge, independent of the exact edge structure and evidence of a QAH gapless edge state. However, the presence of both metallic bulk state and edge state on the 5SL terrace suggests that the edge state hybridizes with the metallic regions formed by these metallic bulk states, and these metallic regions represent continuous conductive pathways that guide the edge state into the bulk, leading to the conductive breakdown of QAHE through dissipative bulk conduction and resulting in non-perfect quantization of Hall conductance and non-zero longitudinal resistance.

To investigate the origin of these metallic regions formed by metallic bulk states, we perform atomic resolution topography and STS maps around the magnetic defects Mn_{Bi} and Bi_{Mn}, which allow us to extract maps of the spatial variation of $E_{g,ex}$, and the gap center energy E_c to determine the influence each defect has on the electronic structure. E_c is equivalent to extrapolating the massive Dirac bands linearly into the gap to obtain the Dirac point in the gapless limit. At locations where the Dirac bands are gapped, E_c is a good measure of local doping shifts associated with the magnetic order. Bi_{Te} defects, are non-magnetic, thus, are unlikely to result in fluctuations in the exchange energy gap $E_{g,ex}$. **Figure 3a** illustrates the position of a Mn_{Bi} defect in the crystal lattice, and Figure 3b shows an atomic resolution image of 10 × 5 nm area (−500 mV, 3 nA) with Mn_{Bi} defects marked in black triangles. The substitution of Bi^{3+} by Mn^{2+} causes contraction on the three neighboring surface Te atoms,[27] therefore, Mn_{Bi} defects in the second Bi^{3+} atomic layer are visible from the surface. The Mn_{Bi} defect density can be estimated to be around 6%, which is very similar to the defect concentration reported in a previous study on MBE-grown $MnBi_2Te_4$ film[29] but is almost double the concentration observed on the surface of a cleaved bulk $MnBi_2Te_4$ crystal.[27] Figure 3c,d are maps of $E_{g,ex}$ and E_c extracted from the dI/dV spectra on the same area in (b) (details found in Figure S4, Supporting Information). Representative dI/dV curves from different locations, marked with $E_{g,ex}$ and E_c values, are plotted in Figure S10, Supporting Information. The Mn_{Bi} defects on the surface (black triangles) are barely visible in the maps of $E_{g,ex}$ and E_c in (c) and (d) respectively, with only small local decrease in $E_{g,ex}$ and slight increase in n-type doping (due to the negative charge of the Mn_{Bi} defects) observed. Instead, the fluctuations in $E_{g,ex}$ and E_c appear to be correlated and to be spatially coherent over length scales of at least a few nanometers, that is, larger than a single defect which is about 0.5 nm. Figure S11, Supporting Information shows the high-resolution DOS maps around the Mn_{Bi} defects in the same area as Figure 3b. The Mn_{Bi} defects are visible in the DOS maps at −0.5 V, but start to diminish as the bias moves toward the exchange gap region. The absence of direct correlation between the distribution of Mn_{Bi} defects and DOS map near the exchange gap is further confirmed by the high-resolution DOS maps (−0.15, −0.12 V) in Figure S11, Supporting Information. Interestingly, the DOS maps at −0.15 and −0.12 V show similarity to the E_c map. Exchange gap histograms of Mn_{Bi} regions and Mn_{Bi} excluded regions are shown in Figure 3e. In regions without Mn_{Bi} defects, the $E_{g,ex}$ histogram is skewed toward a larger gap size when compared to regions with Mn_{Bi} defects, which can be explained by effectively reduced exchange coupling between surface state and magnetic moments due to the AFM interaction between the Mn_{Bi} defects and Mn^{2+} ions. Overall, the patterns of gapped and gapless regions formed over several nanometers are very different from the band gap fluctuations in dilute magnetic doped TIs.[19,31] In dilute magnetic doped TIs, the random distribution of antisites formed by magnetic 3d transition metal ions is directly responsible for the exchange gap fluctuation. But in the current case of 5 SL $MnBi_2Te_4$ thin film, the observed pattern in the $E_{g,ex}$ map appears to be not correlated to distribution of Mn_{Bi} defects, suggesting additional major contribution from magnetic disorder to the gap fluctuations. The origin of the magnetic disorder can be complicated but is very likely to be defect-driven. The local deficiency of Bi p-states on Mn_{Bi} defects could indirectly modulate the weakened intralayer ferromagnetic interaction among Mn^{2+} magnetic moments through non-negligible p–d interactions, as reported by recent magneto-optics and inelastic neutron scattering studies.[39,40] In Figure 3f, a Bi_{Mn} defect in the middle atomic layer is depicted, where the substitution results in the absence of a magnetic moment. Such defects manifest as large bright triangles and are only visible at positive bias as marked by purple triangles in (g). The three bright dots in each triangle are due to Te p-orbitals on the surface responding to Bi_{Mn} defects.[27] dI/dV mapping was performed in the area marked by the yellow box in (g), with the band gap and gap center maps shown in Figure 3h,i. The band gap map in (h) and the histogram in (j) show that the substitution of magnetic Mn^{2+} ions at Bi_{Mn} defects renders the local lattice site non-magnetic and, thus, gapless regions. However, regions well away from the Bi_{Mn} defect still display band gap fluctuation with significant weight of gapless states, suggesting that Bi_{Mn} defects alone do not result in extended regions of suppressed exchange gap and metallicity in the bulk. The results in Figure 3 therefore demonstrate that the exchange gap and gap center fluctuations cannot be explained entirely by local gap suppression due to any of the three types of isolated point defects discussed above. Instead, the results imply the possibility that the longer-ranged collective behavior of magnetic disorder is responsible for the extended exchange gap suppression on the surface of $MnBi_2Te_4$.

To understand the origin of the observed large-scale band gap fluctuations, we perform STS mapping with and without a magnetic field to examine how the extended gapless structures respond to $B_\perp$ field. **Figure 4a** shows STM topography of the atomically flat scan region at $B_\perp$ = 0 T (see Figure S12, Supporting Information for the topography scan taken at 0 T and 1 T where the map region has been carefully aligned using the defects). In Figure 4b STS curves taken at different locations show three types of behavior: gapless regions (blue), gapped regions with fluctuating exchange gap (green and red), and regions where the Dirac

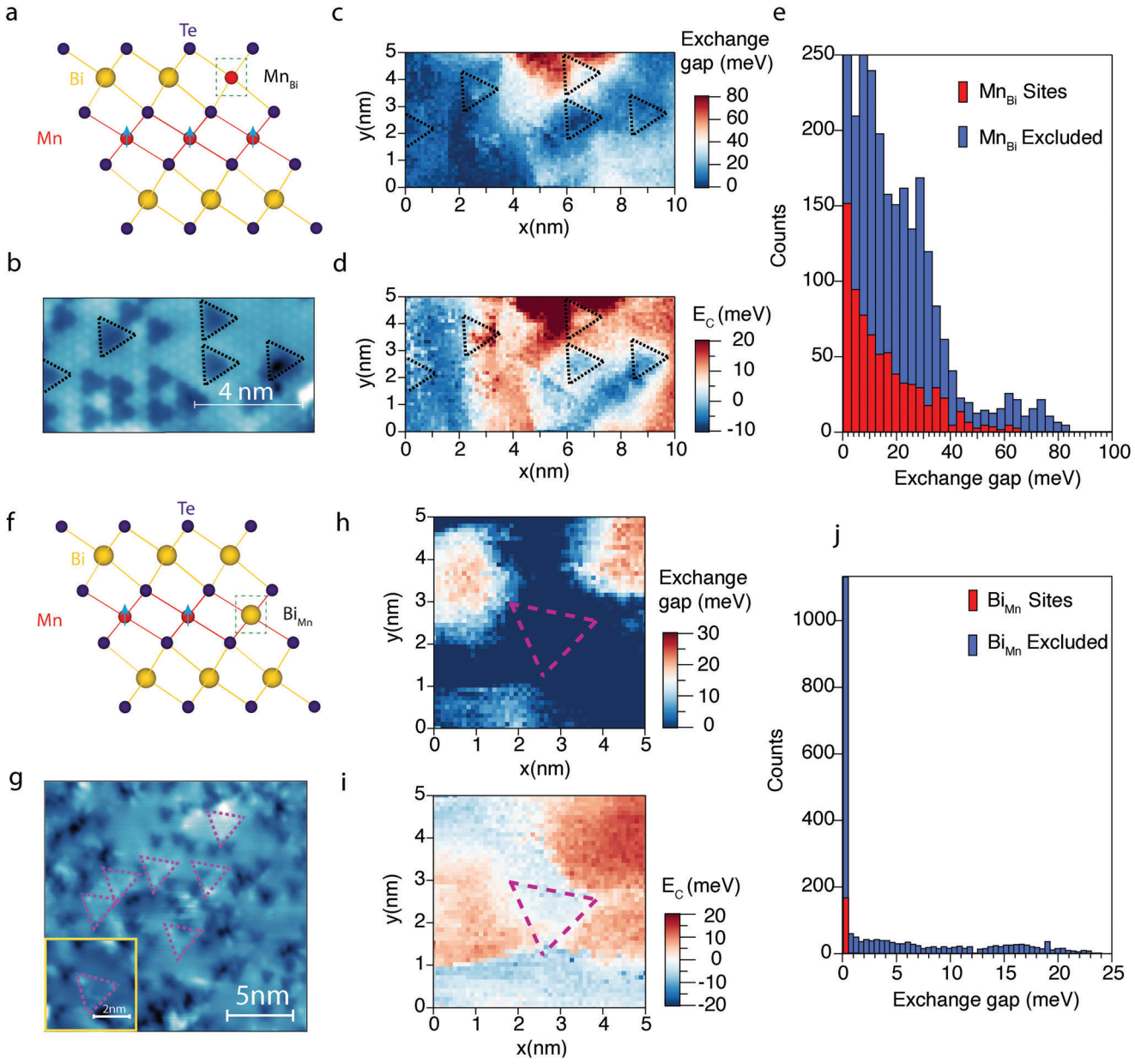

Figure 3. Local response of the exchange gap and doping to point defects. a) Illustration of a Mn_{Bi} defect in the lattice. b) Topography of a 10 × 5 nm area (−500 mV, 3 nA) with Mn_{Bi} defects manifesting as dark triangles (marked in black triangles). c) An exchange gap, $E_{g,ex,}$ map extracted from d*I*/d*V* spectra (−100 mV, 0.8 nA) on a 40 × 80 mesh for visualizing band gap fluctuation and d) gap center from the same region as (c). e) Histograms of the $E_{g,ex}$ extracted from regions with and without Mn_{Bi} defects respectively. f) Illustration of a Bi_{Mn} defect in the lattice. g) Topography of a 40 × 40 nm area (+1.7 eV, 80 pA) with Bi_{Mn} defects which manifest as bigger bright triangles (marked as purple triangles). Insert: h) a 5 × 5 nm region where d*I*/d*V* spectra (−100 mV, 0.91 nA) on a 50 × 50 mesh was taken to show its effect on $E_{g,ex}$ and i) doping level which is reflected on gap center. j) Histograms of $E_{g,ex}$ extracted from the defect region and region excluding the defect.

electron band is suppressed and manifests as an anomalously large bulk gap (orange). Such conduction band (CB) suppression has been previously observed in bulk $MnBi_2Te_4$.[27] The diminished CB intensity prevents us from extracting accurate values of $E_{g,ex}$, thus, the CB-suppressed regions are masked in black in the following gap maps and excluded in the subsequent analysis. The CB-suppressed regions are identified by summing the STS intensity above +20 mV bias at each point and comparing to a summed threshold value of 1.28×10^{-11} for 0 T map and 1.85×10^{-11} for 1 T map that are estimated from STS curves with weak CB intensity and optimized. Figure 4d plots STS curves taken at the same location (purple circle in (a)) at $B_\perp = 0$ T (blue curve) and $B_\perp = 1$ T (red curve). The STS curve is initially gapless at $B_\perp = 0$ T. But it is immediately clear that a 1 T field is sufficient to restore $E_{g,ex}$ to 40 meV with enhanced exchange coupling. Having observed magnetic field-induced band gap modulation, we now

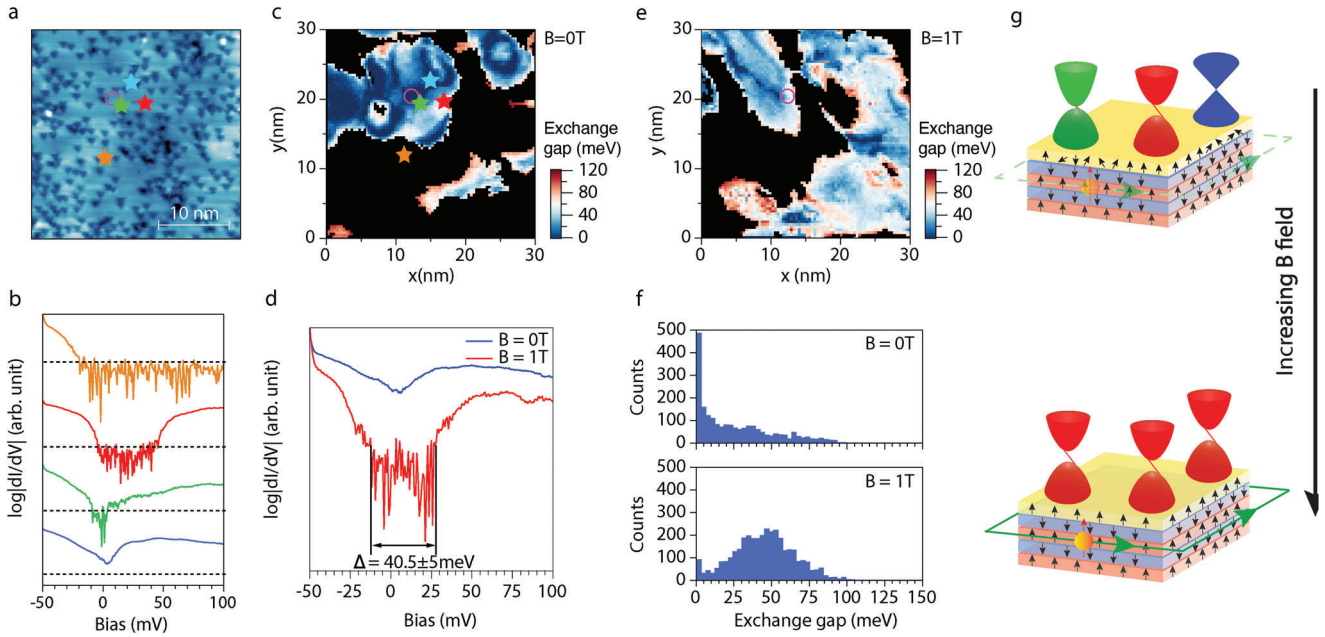

Figure 4. Magnetic field-induced modulation of the exchange gap. a) Topography scan (−0.5 V, 100 pA) of a 30 × 30 nm area where magnetic field-dependent STS measurements were conducted. b) Representative dI/dV spectra taken at different locations, blue: gapless regions, green: reduced-gap regions, red: large-gap regions and orange: regions where Dirac electron band is suppressed which prevents us from extracting the band gap. c) Exchange gap map (80 × 80 points, −150 mV, 400 pA) of the region in (a) at magnetic field $B = 0$ T. d) dI/dV spectra taken at the position marked by purple circle in (a) at $B = 0$ T (blue) and $B = 1$ T (red). An exchange gap of 40.5 meV is opened with 1 T field in a gapless region at 0 T. e) Band gap map (80 × 80 points, −150 mV, 400 pA) of the same region in (a) at $B = 1$ T. Black regions in (c) and (e) correspond to the suppressed Dirac electron band regions which prevent accurate determination of the exchange gap and are excluded from the maps and subsequent histograms in (f). f) Histograms showing exchange gap at $B = 0$ T (upper panel) and $B = 1$ T (lower panel). A clear renormalization of exchange gap is observed in magnetic field. g) Illustration of the exchange gap spatial fluctuation caused by surface magnetic disorder which can be reduced significantly by applying a perpendicular magnetic field. The blue, green, and red Dirac cones represent gapless, partially gapped, and fully gapped regions. Their representative dI/dV curves can be found in Figure 1f. Upon applying a perpendicular magnetic field, the exchange gap in the Dirac cones increases until it reaches saturation.

perform dI/dV mapping (−150 mV, 0.4 nA) on an 80 × 80 point-mesh on the same 30 × 30 nm area in (a) at $B_\perp = 0$ T (Figure 4c) and $B_\perp = 1$ T (Figure 4e). Histograms of $E_{g,ex}$ with and without B field are shown in Figure 4f. These maps reflect the spatial fluctuation of $E_{g,ex}$ over larger scale and will be used to investigate its origin beyond point defects. The histogram in the upper panel of Figure 4f, shows prominent weighting for $E_{g,ex} < 10$ meV, corresponding to a skewed normal distribution (skewness 0.91) with a mean of 26.3 meV and standard deviation of 25.8 meV. Upon applying $B_\perp = 1$ T, the histogram in the lower panel of Figure 4f shows a significant reduction in $E_{g,ex} < 10$ meV regions, and a gap opening and renormalization that results in a near-normal distribution (skewness 0.06) with an increased mean of 44.3 meV and smaller standard deviation of 20.2 meV. A statistical analysis of regions that possess unsuppressed CB intensity at both 0 T and 1 T is presented in Figure S13, Supporting Information. This shows that the average band gap increases by 20.6 meV to a value of 37.8 meV in the 1 T magnetic field and a more bimodal distribution. Additionally, to reveal the gradual change of the $E_{g,ex}$ in low to medium magnetic field, we have performed magnetic field-dependent mapping between 0 and 0.8 T on a different sample, see Figure S14, Supporting Information where the majority of gap renormalization occurs at 0.8 T.

We now consider the possible origins of the extended suppressed gap structures. As recently observed in magnetic force microscopy measurements,[41] whilst the bulk of $MnBi_2Te_4$ thin film remains AFM coupled, the surface exhibits magnetic spin flops which could be enhanced by Bi_{Mn} defects or could change depending on the size of the inter-layer van der Waals gap near the surface.[42] In our thin film $MnBi_2Te_4$ samples, we are able to align the magnetic moments at $B_\perp = 1$ T, much lower than required for inducing surface (2–3.5 T) and bulk spin flops (7.7 T) in previous works,[41,43,44] which indicates that surface spin flop has negligible contribution to the exchange gap fluctuation observed. Additionally, the $B_\perp = 1$ T for restoring the exchange gap partially is negligibly small compared to the field for aligning the magnetic moments from Mn_{Bi} anti-sites,[45] implying the exchange gap fluctuation is not likely to originate from Mn_{Bi} in the deeper layers. Otherwise, there should be minimal change in the exchange gap size in the 1 T magnetic field. This suggests that there is a significant magnetic disorder most likely in the first SL, a magnetic uncompensated layer, that causes band gap fluctuation on the nanometer scale.[25] Such magnetic disorder occurs in the Mn^{2+} layer located at the center of the top SLs, which is very hard to probe using STM. However, the exchange interaction of the Dirac states with Mn^{2+} ions enables indirect mapping of such magnetic disorder based on the suppression of $E_{g,ex}$ as seen in Figure 4c,e.

Figure 4g illustrates the situation schematically. Magnetic disorder causes local suppression of the exchange gap (blue gapless Dirac spectrum) in extended regions due to long-range exchange interactions among local moments, while some regions retain

partial (green band structure) or full (red band structure) gaps. In regions with vanishing exchange gap, the QAH edge state in the vicinity is no longer protected by the gapped bulk topological phase with a non-zero Chern number. Otherwise, such topological protection offers robustness against perturbations less than the magnitude of the exchange gap. Application of $B_{\perp}$ = 1 T (bottom) aligns the moments of magnetically disordered regions, increasing the gap (red band structure). Interestingly, the B field also reduces the area of suppressed CB regions, suggesting CB suppression is also related to disordered magnetic moments beyond the influence of deficient Bi orbitals due to Mn_{Bi} defects.[27] Finally, we propose an explanation to the origin of the magnetic disorder. The prevalent band gap fluctuation observed implies weakened inter-layer and intra-layer exchange interaction in 5 SL $MnBi_2Te_4$. Its low magnetic anisotropy energy makes $MnBi_2Te_4$ similar to a 2D Heisenberg magnet that does not sustain long-range ferromagnetic order.[40,44,46] Such weakened magnetic anisotropy makes the magnetic ordering more vulnerable to magnetic defects, especially Bi_{Mn}. With Mn^{2+} ions replaced by non-magnetic Bi^{3+} ions, exchange coupling between intra-layer Mn^{2+} ions is weakened, depending on the concentration of such defects. Although, the direct exchange coupling between Mn_{Bi} and surface states is much weaker as discussed in Figure 3, Mn_{Bi} can still cause local deficiency of Bi p-orbitals and indirectly influence the magnetic moments in the middle of SL by p–d interaction. Therefore, the ferromagnetic configuration of Mn^{2+} ions could be canted and disordered in the presence of a large amount of anti-site defects, resulting in reduced magnetization and gapless spectra over extended areas. A recent quasiparticle interference study on cleaved $MnBi_2Te_4$ favors this explanation and a similar mechanism has also been reported by Liu et al.[29,47] Last, we present an $E_{g,ex}$ map of a region with larger amount of Bi_{Mn} defects in 0 T and 1 T magnetic field in Figure S15, Supporting Information. This region is indeed mostly gapless. Upon applying the 1 T field, a significant reduction of gapless regions occurs (further details in Figure S15, Supporting Information). CB suppression is almost absent in this region, which can be explained by the large amount of Bi_{Mn} defects that offer sufficient p-states to form Dirac bands. It is worthwhile to mention that because of the unique sensitivity of STM/STS to surface features, relating the observed exchange gap fluctuation to defects throughout the thin film is very challenging. Nevertheless, the STM/STS measurements performed in this work clearly demonstrate fluctuation and sensitivity of the exchange gap to magnetic field on the surface.

3. Conclusion

Using magnetic field STM/STS measurements, we have demonstrated that the gapless edge state in QAHI 5 SL $MnBi_2Te_4$ is directly coupled to extended percolating bulk metallic regions arising from band gap fluctuations caused by magnetic surface disorder. By applying a magnetic field, the band gap fluctuations can be greatly reduced, and the average exchange gap increases to 44 meV, close to predicted values for 5 SL $MnBi_2Te_4$.[21,22,32] These results provide insight on the mechanism of topological breakdown and how it can be restored in a magnetic field.[23,48] A recent study on a 7 SL $MnBi_2Te_4$ flake device using scanning superconducting quantum interference device measurements discovered the coexistence of chiral edge state and bulk state conduction. They find edge-bulk scattering on the micrometer scale, which shows striking similarity to our discovery and supports our claims on the breakdown mechanism.[49] Minimizing magnetic disorder will be the key to realizing QAHE in not only odd-layer $MnBi_2Te_4$ ultra-thin films but also other MTIs at elevated temperature in the future. The weak interlayer interaction and intralayer ferromagnetic ground state close to instability limit in $MnBi_2Te_4$ makes it difficult to sustain long-range magnetic order, especially with significant amounts of anti-site defects, and improved $MnBi_2Te_4$ crystal or film growth alone may not be sufficient to fully mitigate magnetic disorder. Therefore, other strategies such as heterostructure engineering $MnBi_2Te_4$ with other robust, highly anisotropic 2D ferromagnets[50] or ferromagnetic/topological insulators sandwich heterostructures[51–53] may be required to achieve the robust topological protection required for next-generation lossless electronics and topological quantum computing.[6–9]

4. Experimental Section

Growth of Ultra-Thin $MnBi_2Te_4$ on Si(111): Ultra-thin $MnBi_2Te_4$ thin films were grown in a Scienta Omicron Lab 10 MBE growth chamber. The Si (111) substrate was flash-annealed at 1180 °C with direct current heating to achieve an atomically flat (7 × 7) surface reconstruction. Effusion cells were used to evaporate elemental Mn (99.9%), Bi (99.999%), and Te (99.95%). A quartz crystal microbalance was used to calibrate rates before growth and reflection high-energy electron diffraction (RHEED) was used to monitor the crystal growth in situ. Each SL of $MnBi_2Te_4$ was grown by first growing 1 quintuple-layer Bi_2Te_3 followed by growing a bilayer MnTe in overflux of Te at 230 °C. 1 SL $MnBi_2Te_4$ forms spontaneously by re-arranging MnTe layer into the middle of 1QL Bi_2Te_3 similar to $MnBi_2Se_4$.[54] The growth time for each 1 QL Bi_2Te_3 and MnTe was calibrated from the oscillation of the RHEED pattern. Then the process was repeated five times to reach the desired thickness and finished with a post-annealing process in Te flux for 10 min to improve crystallinity. The films were subsequently capped with 10 nm amorphous Te, to allow transfer in air to the STM chamber.

STM/STS Measurements: The capped films grown on boron-doped silicon (111) (resistivity 0.1–0.2 Ω · cm) were transferred in air to a Createc LT-STM chamber and were annealed in ultra-high vacuum at 290 °C for 2.5 h to remove the Te capping before performing STM measurements at 4.3 K. A Pt-Ir tip was prepared and calibrated using an Au (111) single crystal, confirming the presence of the Shockley surface state at −0.5 V and flat LDOS near the Fermi level before all measurements. The STM differential conductance measurements (dI/dV) were performed using standard lock-in method with 5 mV AC excitation voltage at 797 Hz for exchange gap mapping and 2 mV AC excitation voltage at 797 Hz for edge state mapping. Differential conductance measurements were made under open feedback conditions with the tip in a fixed position above the surface. For the magnetic field-dependent STM/STS measurements, a magnetic field up to 1 T was applied perpendicular to the sample.

ARPES Measurements: ARPES measurements were performed at Beamline 10.0.1 at Advanced Light Source in Lawrence Berkeley National Laboratory, USA. A 5 SL $MnBi_2Te_4$ sample was grown on antimony doped silicon (111) substrate (resistivity 0.1–0.2 Ω · cm) following the same growth procedure in an MBE system integrated with the beamline endstation and transferred into the measurement chamber after growth. Data was taken using a Scienta R4000 analyzer at 8K and a photon energy of 50 eV was selected to optimize the signal. The combined energy resolution was 15–20 meV and the angular resolution was 0.2°, or equivalent to 0.01$Å^{-1}$ momentum resolution for the photon energy used. The ARPES spectra in the supporting information were performed on a home-build

toroidal analyser using a He lamp at the Soft-Xray beamline at the Australian Synchrotron.

Statistical Analysis: The histograms for exchange gaps were obtained from exchange gap maps with a bin size of 3 meV. The sample size for the histogram can be calculated from the mesh size which is included in the caption for each exchange gap map. The Mn_{Bi} defect excluded map in Figure 3 was obtained by applying a mask to the exchange gap map. The mask was obtained by identifying each dark triangle in the topography scan. Statistical analysis and ARPES spectrum analysis were performed using Igor Pro 7. STS map analysis was performed using Python and Igor Pro 7. All STM images were processed using Gwyddion.

Supporting Information

Supporting Information is available from the Wiley Online Library or from the author.

Acknowledgements

Q.L., I.D.B., A.D.C., M.S.F., and M.T.E. acknowledge funding support from ARC Centre for Future Low Energy Electronics Technologies (FLEET) CE170100039. M.T.E. acknowledges funding support from ARC Future Fellowship FT2201000290. Q.L. acknowledges funding support from the AINSE postgraduate award. This research used resources of the Advanced Light Source, which is a DOE Office and Science User Facility under contract no. DE-AC02-05CH11231. Q.L. and M.T.E. acknowledge travel funding provided by the International Synchrotron Access Program (ISAP) managed by the Australian Synchrotron, part of ANSTO, and funded by the Australian Government. Part of this research was undertaken on the soft X-ray beamline at the Australian Synchrotron, a division of ANSTO. J.H. was supported by the National Research Foundation of Korea (NRF) grant funded by Korean government (MSIT) (RS-2023-00280346) and the GRDC (Global REsearch Development Center) Cooperative Hub Program through the NRF funded by the Ministry of Science and ICT (MIST) (RS-2023-00258359). This work was performed in part at the Melbourne Centre for Nanofabrication (MCN), the Victorian Node of the Australian National Fabrication Facility (ANFF).

Open access publishing facilitated by Monash University, as part of the Wiley - Monash University agreement via the Council of Australian University Librarians.

Conflict of Interest

The authors declare no conflict of interest.

Author Contributions

Q.L. and M.T.E. devised the STM experiments. Q.L. performed the MBE growth and STM/STS measurements at Monash University. I.D.B., A.D.C., L.W., B.L., and T.-H.-Y.V. assisted with the scanning probe measurements. M.T.H.B., M.Z., A.T., C.X.T., J.H., and S.-K.M. assisted the ARPES measurements. Q.L. performed data analysis with assistance from J.M., D.M., M.S.F., and M.T.E. Q.L. and M.T.E. composed the manuscript. All authors read the manuscript and contributed feedback.

Data Availability Statement

The data that support the findings of this study are available from the corresponding author upon reasonable request.

Keywords

magnetic topological insulators, quantum anomalous Hall effect, scanning tunneling microscopy and spectroscopy, topological materials

Received: November 12, 2023
Revised: February 20, 2024
Published online:

[1] F. Schindler, Z. Wang, M. G. Vergniory, A. M. Cook, A. Murani, S. Sengupta, A. Y. Kasumov, R. Deblock, S. Jeon, I. Drozdov, H. Bouchiat, S. Guéron, A. Yazdani, B. A. Bernevig, T. Neupert, *Nat. Phys.* **2018**, *14*, 918.
[2] F. Reis, G. Li, L. Dudy, M. Bauernfeind, S. Glass, W. Hanke, R. Thomale, J. Schäfer, R. Claessen, *Science* **2017**, *357*, 287.
[3] Y. Tanaka, Z. Ren, T. Sato, K. Nakayama, S. Souma, T. Takahashi, K. Segawa, Y. Ando, *Nat. Phys.* **2012**, *8*, 800.
[4] C. Liu, Y. Wang, H. Li, Y. Wu, Y. Li, J. Li, K. He, Y. Xu, J. Zhang, Y. Wang, *Nat. Mater.* **2020**, *19*, 522.
[5] M. Z. Hasan, C. L. Kane, *Rev. Mod. Phys.* **2010**, *82*, 3045.
[6] A. J. Bestwick, E. J. Fox, X. Kou, L. Pan, K. L. Wang, D. Goldhaber-Gordon, *Phys. Rev. Lett.* **2015**, *114*, 187201.
[7] C.-Z. Chang, W. Zhao, D. Y. Kim, H. Zhang, B. A. Assaf, D. Heiman, S.-C. Zhang, C. Liu, M. H. W. Chan, J. S. Moodera, *Nat. Mater.* **2015**, *14*, 473.
[8] B. Lian, X.-Q. Sun, A. Vaezi, X.-L. Qi, S.-C. Zhang, *Proc. Natl. Acad. Sci. USA* **2018**, *115*, 10938.
[9] X.-L. Qi, T. L. Hughes, S.-C. Zhang, *Phys. Rev. B* **2010**, *82*, 184516.
[10] B. Huckestein, *Rev. Mod. Phys.* **1995**, *67*, 357.
[11] S. L. Sondhi, S. M. Girvin, J. P. Carini, D. Shahar, *Rev. Mod. Phys.* **1997**, *69*, 315.
[12] N. Moreau, B. Brun, S. Somanchi, K. Watanabe, T. Taniguchi, C. Stampfer, B. Hackens, *Nat. Commun.* **2021**, *12*, 4265.
[13] A. Marguerite, J. Birkbeck, A. Aharon-Steinberg, D. Halbertal, K. Bagani, I. Marcus, Y. Myasoedov, A. K. Geim, D. J. Perello, E. Zeldov, *Nature* **2019**, *575*, 628.
[14] J. Maciejko, C. Liu, Y. Oreg, X.-L. Qi, C. Wu, S.-C. Zhang, *Phys. Rev. Lett.* **2009**, *102*, 256803.
[15] C. Liu, D. Culcer, Z. Wang, M. T. Edmonds, M. S. Fuhrer, *Nano Lett.* **2020**, *20*, 6306.
[16] C. L. Kane, E. J. Mele, *Phys. Rev. Lett.* **2005**, *95*, 226801.
[17] L. Fu, C. L. Kane, E. J. Mele, *Phys. Rev. Lett.* **2007**, *98*, 106803.
[18] M. Liu, W. Wang, A. R. Richardella, A. Kandala, J. Li, A. Yazdani, N. Samarth, N. P. Ong, *Sci. Adv.* **2016**, *2*, 1600167.
[19] I. Lee, C. K. Kim, J. Lee, S. J. L. Billinge, R. Zhong, J. A. Schneeloch, T. Liu, T. Valla, J. M. Tranquada, G. Gu, J. C. S. Davis, *Proc. Natl. Acad. Sci. USA* **2015**, *112*, 1316.
[20] M. M. Otrokov, I. I. Klimovskikh, H. Bentmann, D. Estyunin, A. Zeugner, Z. S. Aliev, S. Gaß, A. U. B. Wolter, A. V. Koroleva, A. M. Shikin, M. Blanco-Rey, M. Hoffmann, I. P. Rusinov, A. Y. Vyazovskaya, S. V. Eremeev, Y. M. Koroteev, V. M. Kuznetsov, F. Freyse, J. Sánchez-Barriga, I. R. Amiraslanov, M. B. Babanly, N. T. Mamedov, N. A. Abdullayev, V. N. Zverev, A. Alfonsov, V. Kataev, B. Büchner, E. F. Schwier, S. Kumar, et al., *Nature* **2019**, *576*, 416.
[21] J. Li, Y. Li, S. Du, Z. Wang, B.-L. Gu, S.-C. Zhang, K. He, W. Duan, Y. Xu, *Sci. Adv.* **2019**, *5*, eaaw5685.
[22] M. M. Otrokov, I. P. Rusinov, M. Blanco-Rey, M. Hoffmann, A. Y. Vyazovskaya, S. V. Eremeev, A. Ernst, P. M. Echenique, A. Arnau, E. V. Chulkov, *Phys. Rev. Lett.* **2019**, *122*, 107202.
[23] Y. Deng, Y. Yu, M. Z. Shi, Z. Guo, Z. Xu, J. Wang, X. H. Chen, Y. Zhang, *Science* **2020**, *367*, 895.
[24] Y. Bai, Y. Li, J. Luan, R. Liu, W. Song, Y. Chen, P.-F. Ji, Q. Zhang, F. Meng, B. Tong, L. Li, Y. Jiang, Z. Gao, L. Gu, J. Zhang, Y. Wang, Q.-K. Xue, K. He, Y. Feng, X. Feng, *Natl. Sci. Rev.* **2023**, *11*, nwad189.
[25] K. F. Garrity, S. Chowdhury, F. M. Tavazza, *Phys. Rev. Mater.* **2021**, *5*, 024207.

[26] Y. Yuan, X. Wang, H. Li, J. Li, Y. Ji, Z. Hao, Y. Wu, K. He, Y. Wang, Y. Xu, W. Duan, W. Li, Q.-K. Xue, *Nano Lett.* **2020**, *20*, 3271.
[27] Z. Huang, M.-H. Du, J. Yan, W. Wu, *Phys. Rev. Mater.* **2020**, *4*, 121202.
[28] M. Garnica, M. M. Otrokov, P. C. Aguilar, I. I. Klimovskikh, D. Estyunin, Z. S. Aliev, I. R. Amiraslanov, N. A. Abdullayev, V. N. Zverev, M. B. Babanly, N. T. Mamedov, A. M. Shikin, A. Arnau, A. L. V. de Parga, E. V. Chulkov, R. Miranda, *npj Quantum Mater.* **2022**, *7*, 7.
[29] M. Liu, C. Lei, H. Kim, Y. Li, L. Frammolino, J. Yan, A. H. Macdonald, C.-K. Shih, *Proc. Natl. Acad. Sci. USA* **2022**, *119*, 2207681119.
[30] Y. S. Hor, P. Roushan, H. Beidenkopf, J. Seo, D. Qu, J. G. Checkelsky, L. A. Wray, D. Hsieh, Y. Xia, S. Y. Xu, D. Qian, M. Z. Hasan, N. P. Ong, A. Yazdani, R. J. Cava, *Phys. Rev. B* **2010**, *81*, 195203.
[31] H. Beidenkopf, P. Roushan, J. Seo, L. Gorman, I. Drozdov, Y. S. Hor, R. J. Cava, A. Yazdani, *Nat. Phys.* **2011**, *7*, 939.
[32] C. X. Trang, Q. Li, Y. Yin, J. Hwang, G. Akhgar, I. Di Bernardo, A. Grubišić-Čabo, A. Tadich, M. S. Fuhrer, S.-K. Mo, N. V. Medhekar, M. T. Edmonds, *ACS Nano* **2021**, *15*, 13444.
[33] E. D. L. Rienks, S. Wimmer, J. Sánchez-Barriga, O. Caha, P. S. Mandal, J. Růžička, A. Ney, H. Steiner, V. V. Volobuev, H. Groiss, M. Albu, G. Kothleitner, J. Michalička, S. A. Khan, J. Minár, H. Ebert, G. Bauer, F. Freyse, A. Varykhalov, O. Rader, G. Springholz, *Nature* **2019**, *576*, 423.
[34] F. Lüpke, A. D. Pham, Y.-F. Zhao, L.-J. Zhou, W. Lu, E. Briggs, J. Bernholc, M. Kolmer, J. Teeter, W. Ko, C.-Z. Chang, P. Ganesh, A.-P. Li, *Phys. Rev. B* **2022**, *105*, 035423.
[35] H.-K. Xu, M. Gu, F. Fei, Y.-S. Gu, D. Liu, Q.-Y. Yu, S.-S. Xue, X.-H. Ning, B. Chen, H. Xie, Z. Zhu, D. Guan, S. Wang, Y. Li, C. Liu, Q. Liu, F. Song, H. Zheng, J. Jia, *ACS Nano* **2022**, *16*, 9810.
[36] J. Jia, E. Marcellina, A. Das, M. S. Lodge, B. Wang, D.-Q. Ho, R. Biswas, T. A. Pham, W. Tao, C.-Y. Huang, H. Lin, A. Bansil, S. Mukherjee, B. Weber, *Nat. Commun.* **2022**, *13*, 6046.
[37] Z. Alpichshev, J. G. Analytis, J. H. Chu, I. R. Fisher, Y. L. Chen, Z. X. Shen, A. Fang, A. Kapitulnik, *Phys. Rev. Lett.* **2010**, *104*, 016401.
[38] J. L. Collins, A. Tadich, W. Wu, L. C. Gomes, J. N. B. Rodrigues, C. Liu, J. Hellerstedt, H. Ryu, S. Tang, S.-K. Mo, S. Adam, S. A. Yang, M. S. Fuhrer, M. T. Edmonds, *Nature* **2018**, *564*, 390.
[39] H. Padmanabhan, V. A. Stoica, P. K. Kim, M. Poore, T. Yang, X. Shen, A. H. Reid, M.-F. Lin, S. Park, J. Yang, H. Wang, N. Z. Koocher, D. Puggioni, A. B. Georgescu, L. Min, S. H. Lee, Z. Mao, J. M. Rondinelli, A. M. Lindenberg, L.-Q. Chen, X. Wang, R. D. Averitt, J. W. Freeland, V. Gopalan, *Adv. Mater.* **2022**, *34*, 2202841.
[40] B. Li, J. Q. Yan, D. M. Pajerowski, E. Gordon, A. M. Nedić, Y. Sizyuk, L. Ke, P. P. Orth, D. Vaknin, R. J. McQueeney, *Phys. Rev. Lett.* **2020**, *124*, 167204.
[41] P. M. Sass, J. Kim, D. Vanderbilt, J. Yan, W. Wu, *Phys. Rev. Lett.* **2020**, *125*, 037201.
[42] A. Shikin, T. Makarova, A. Eryzhenkov, D. Y. Usachov, D. Estyunin, D. Glazkova, I. Klimovskikh, A. Rybkin, A. Tarasov, *arXiv:2205.07501* **2022**.
[43] S. K. Bac, K. Koller, F. Lux, J. Wang, L. Riney, K. Borisiak, W. Powers, M. Zhukovskyi, T. Orlova, M. Dobrowolska, J. K. Furdyna, N. R. Dilley, L. P. Rokhinson, Y. Mokrousov, R. J. McQueeney, O. Heinonen, X. Liu, B. A. Assaf, *npj Quantum Mater.* **2022**, *7*, 46.
[44] S. Yang, X. Xu, Y. Zhu, R. Niu, C. Xu, Y. Peng, X. Cheng, X. Jia, Y. Huang, X. Xu, J. Lu, Y. Ye, *Phys. Rev. X* **2021**, *11*, 011003.
[45] Y. Lai, L. Ke, J. Yan, R. D. McDonald, R. J. McQueeney, *Phys. Rev. B* **2021**, *103*, 184429.
[46] K. He, Q.-K. Xue, *SPIN* **2019**, *09*, 1940016.
[47] Q. Bian, Z. Shao, R. Song, Y. Cao, Y. Hou, S. Li, R. Zhai, X. Li, F. Zheng, W. Zhu, Y. Ou, P. Zhang, M. Pan, *Mater. Today Electron.* **2023**, *5*, 100050.
[48] Y. Bai, Y. Li, J. Luan, R. Liu, W. Song, Y. Chen, P.-F. Ji, Q. Zhang, F. Meng, B. Tong, *arXiv:2206.03773* **2022**.
[49] J. Zhu, Y. Feng, X. Zhou, Y. Wang, Z. Lian, W. Lin, Q. L. He, Y. Lin, Y.-L. Wang, H. Yao, H. Li, Y. Wu, J. Wang, J. Shen, J. Zhang, Y. Wang, Y. Wang, *arXiv:2307.10150* **2023**.
[50] H. Fu, C.-X. Liu, B. Yan, *Sci. Adv.* **2020**, *6*, eaaz0948.
[51] M. M. Otrokov, T. V. Menshchikova, M. G. Vergniory, I. P. Rusinov, A. Y. Vyazovskaya, Y. M. Koroteev, G. Bihlmayer, A. Ernst, P. M. Echenique, A. Arnau, E. V. Chulkov, *2D Mater.* **2017**, *4*, 025082.
[52] Q. Li, C. X. Trang, W. Wu, J. Hwang, D. Cortie, N. Medhekar, S.-K. Mo, S. A. Yang, M. T. Edmonds, *Adv. Mater.* **2022**, *34*, 2107520.
[53] S. Bhattacharyya, G. Akhgar, M. Gebert, J. Karel, M. T. Edmonds, M. S. Fuhrer, *Adv. Mater.* **2021**, *33*, 2007795.
[54] T. Zhu, A. J. Bishop, T. Zhou, M. Zhu, D. J. O'Hara, A. A. Baker, S. Cheng, R. C. Walko, J. J. Repicky, T. Liu, J. A. Gupta, C. M. Jozwiak, E. Rotenberg, J. Hwang, I. Žutić, R. K. Kawakami, *Nano Lett.* **2021**, *21*, 5083.